CHALMERS
UNIVERSITY OF TECHNOLOGY

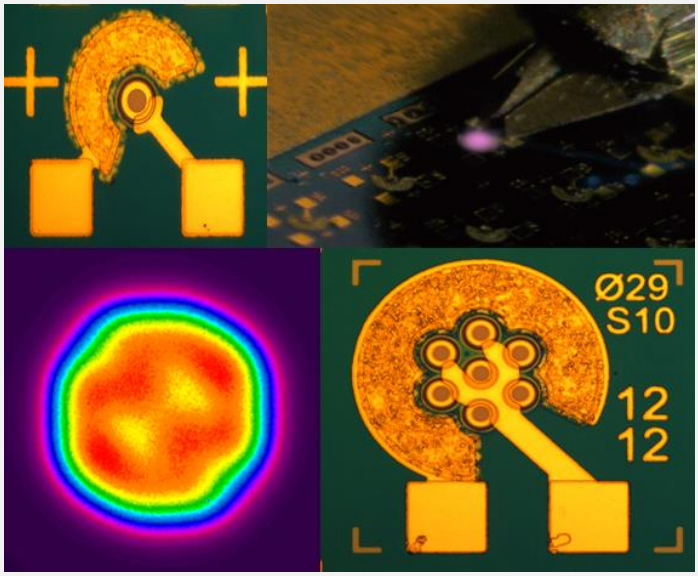

Modal characterization of 940 nm VCSELs

For 3D-sensing and LiDAR application

Master's thesis in Photonics Engineering

SAHAR FARAJZADEH

DEPARTMENT OF Microtechnology and Nanoscience – MC2
CHALMERS UNIVERSITY OF TECHNOLOGY
Gothenburg, Sweden 2021

MASTER'S THESIS 2021

Modal characterization of 940 nm VCSELs for 3D-sensing and LiDAR application

Sahar Farajzadeh

CHALMERS
UNIVERSITY OF TECHNOLOGY

Department of Microtechnology and Nanoscience
Photonics Laboratory
Optoelectronics
CHALMERS UNIVERSITY OF TECHNOLOGY
Göteborg, Sweden 2021

Modal characterization of 940 nm VCSELs for 3D-sensing and LiDAR application
SAHAR FARAJZADEH

Supervisor: Prof. Anders Larsson, and Mehdi Jahed
Department of Microtechnology and Nanoscience
Examiner: Prof. Anders Larsson

Master's Thesis 2021
Photonics Laboratory
Chalmers University of Technology
SE-41296 Göteborg
Sweden
Telephone +46 (0)31-772 1000

Cover: Modal characterization of 940 nm VCSELs for 3D-sensing and LiDAR applications

Printed by Chalmers Tryckeri-Reproservice
Göteborg, Sweden 2021

Modal characterization of 940 nm VCSELs for 3D-sensing and LiDAR applications
SAHAR FARAJZADEH
Department of Microtechnology and Nanoscience
Chalmers University of Technology

Abstract

Due to increasing demands in 3D-sensing solutions, e.g. face recognition in mobiles and light detection and ranging (LiDAR) in autonomous cars, 940 nm vertical-cavity surface-emitting lasers (VCSELs) as unique light sources play an essential role in industrial utilizations. Therefore, it is necessary to study the modal characterization of 940 nm VCSELs with considering various physical parameters to meet the required usage situations. Self-heating and temperature dependence of these devices are the most important factors that affects the performance of the 3D-sensing. In this thesis, VCSELs with different oxide aperture diameters have been studied. For each VCSEL, output power and voltage as a function of bias current (IPV), optical spectrum and 2D far-field mode profile were measured. All measurements were done at different temperatures and under continues-wave (CW) and pulse current operations. Finally, the output data are analysed and reported in this thesis.

Keywords: VCSELs, CW current, Pulsed current, IPV performance, Optical spectrum, Modal characterization, 3D-sensing, and LiDAR.

Acknowledgements

There have been many supportive people who helped me a lot leading me up to this thesis project.
I would first like to thank my supervisor and examiner Prof. Anders Larsson for letting me to work on this interesting field and for his friendly support and great respect. I also would like to thank Mehdi Jahed for his great supervision and his valuable time and patience for having fruitful discussions in every step of this project. I am very lucky to have his great support and love as my partner and supervisor. Studying on VCSELs with respect to LiDAR and sensing applications was very exciting and ideal for me. However, I am very happy that I could do it in such a friendly lab which I really want to thank all of Photonics Lab members that have made spending time very joyful for me there. I would also like to thank Nvidia (OptiGot) and Erik Haglund for fabricating the 6B9 0940-8 VCSELs which were used in this thesis project. The last but not least, many thanks to my family for their great support from miles away but always in my heart.

Sahar Farajzadeh
Göteborg
June 2021

Contents

Abbreviations and notations vii
1. Introduction 1
2. Theory 3
2.1 VCSEL fundamentals 3
2.1.1 VCSEL features and applications 5
2.2 Optical resonant cavities 6
2.3 Near-field and far-field 6
2.4 Single/Multimode VCSELs 7
2.5 Modal properties 7
2.6 Beam width and divergence 7
2.6.1 Focal length method 9
2.6.2 Far-field wide angle method 9
2.6.3 Far-field two points 9
2.7 Why 940 nm VCSELs? 9
3. Methods 11
3.1 IPV measurements setup with integrating sphere 11
3.2 Spectrum measurement with lens coupled setup 12
3.3 Beam profile with WB-I and CCD camera 13
4. Results 15
4.1 Characterization of VCSELs with CW current operation 15
4.2 Characterization of VCSELs with pulsed current operation 24
4.3 Beam profiles 27
5. Conclusion 31
6. Bibliography 33
7. List of VCSELs 35

Abbreviations and notations

VCSEL	Vertical-cavity surface-emitting lasers
Laser	Light amplification by stimulated emission radiation
CCD	Charge coupled device
CW	Continuous wave
MBE	Molecular beam epitaxy
MOCVD	Metal organic chemical vapor deposition
DBR	Distributed Bragg reflectors
QW	Quantum well
3D	Three dimensional
LiDAR	Light detection and ranging
IPV	Current- Power- Voltage
WB-I	Wide beam imager
∅	Oxide aperture
LP	Linear polarization
FWHM	Full wave half maximum
DC	Duty cycle
ISO	International organization for standardization
MMF	Multi-mode fiber
NA	Numerical aperture
OSA	Optical spectrum analyser
mW	Milli watt
mA	Milli amper
P_{diss}	Dissipated power
R_{th}	Thermal impedance
ND	Neutral density (Filter or optical attenuator)
D4σ	Four times the standard deviation of the energy distribution
PW	Pulse width

1. Introduction

Vertical-cavity surface-emitting lasers (VCSELs) have been greatly used as an illumination source in optical interconnects [1] and IR applications e.g. data centres and 3D-sensing applications (face recognition, LiDAR, and drive assistance systems) [2]. The way we use Internet via smart phones, tablets and computer has recently dramatically changed which led to the concept of cloud computing. The main outreach is that not only there is no necessity to have out data saved on device but also, they can be used as terminals to have access to servers in data centres [3]. On the other hand, VCSELs have very novel and hot specific application in 3D-sensing embracing face recognition, 3D-movements, 3D-imaging [2] and LiDAR, etc [4]. Fascinating characteristics, small volume, competitive pricing, low beam divergence [5], speed, reliability, efficiency [6], easy integration and possibility to fabricate the VCSEL-based modules with compact form-factor [2] that led VCSEL to show remarkable improvements in comparing to other methods. This makes VCSEL ideal for consumer and new application's market. In addition, VCSEL singlets and arrays can provide power required for a few millimeters up to a few hundred meters distances [4].

This thesis will concentrate on modal characterization of 940 nm VCSELs with different oxide aperture sizes. In order to compare characteristics of VCSELs under harsh environment (different temperatures) with considering self-heating, several setups are used such as IPV measurement (current-power-voltage) with integrating sphere, optical spectrum measurement with lens coupled setup, imager setup for measuring far-field modal distribution with WB-I (wide beam imager) and CCD camera in CW (continues wave) current operations. In addition, to avoid self-heating and to increase power of the VCSELs and also to be used in a time-of-flight LiDAR, VCSELs are studied under pulsed source and characterized with the same setups.

The thesis consists of five main chapters which covers introduction and outline of the thesis, theoretical background, the methods of measurements and setups used during the thesis. Then, the results of measurements are presented and discussed in chapter 4. Finally, the thesis is concluded in chapter 5.

2. Theory

2.1 VCSEL fundamentals

Literally, VCSEL stands for vertical-cavity surface-emitting laser where the emission is normal to the surface with lasing in a vertical cavity [3]. All lasers have a kind of resonator which is simply like a Fabry-Perot laser resonance system as is illustrated in figure 2.1. It contains two parallel mirrors. One of the mirrors (R_1) is usually designed for ~100% reflectivity while the output mirror has less reflectivity (R_2).

Figure 2.1: A simple form of the Fabry-Perot laser system

Regarding the light and matter interactions, there are three different actions including absorption, spontaneous and stimulated emissions, figure 2.2. When a photon with energy of $\Delta E=E_2-E_1=h\vartheta$ (h is Plank's constant and ϑ is photon frequency) is radiated to a group of atoms, there is a possibility of absorption by electron in the ground level which results in transferring the electron to the excited level. In currents below threshold current (low currents), the radiation is due to the spontaneous emissions (where electrons in the excited level relax to the ground level) with different wavelengths, phases and polarization states which has dramatically low power and intensity in comparison with the stimulated emission. However, there is an external energy induction equal to ΔE in stimulated emission. This results in relaxation of the electron in excited level with output of two coherent and in-phase photons with same polarization states, energy, and direction.

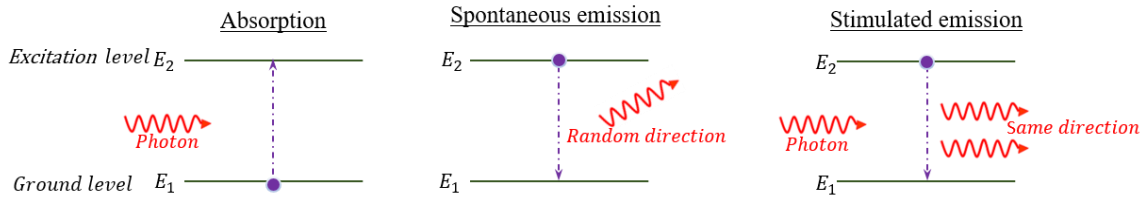

Figure2.2: Light-matter interactions including absorption, spontaneous and stimulated emissions.

A cross section of a VCSEL is shown in figure 2.3. A VCSEL is like a Fabry Perot laser with two mirrors and a sandwiched active region (gain medium). The mirrors are DBRs, distributed Bragg reflectors, with 20-40 layers of two different materials grown by epitaxial method e.g. molecular beam

epitaxy (MBE) or metal-organic chemical vapor deposition (MOCVD). VCSELs fabricated in Optoelectronics Group of Chalmers University of Technology, are GaAs-based with various compositions of $Al_xGa_{1-x}As$ to form the DBRs. Usually, the upper and lower DBRs are p-doped and n-doped AlGaAs, respectively, to create a diode junction and population inversion that is required for lasing. The top and bottom DBRs are designed to provide reflectivity of ~99% and ~99.9%, respectively. Gain medium in VCSELs consists of a few quantum wells (QWs) of a narrow bandgap material, e.g. InGaAs, positioned between wide bandgap material, e.g. $Al_xGa_{1-x}As$ or GaAsP. High Al-content layer just above the QWs forms oxide aperture with higher refractive index which confines injected electrical current and transverse optical filed by its transverse effective index profile. For the lasing to occur, not only the phase of the optical filed must repeat itself after one round-trip inside the cavity (resonance condition), but also the optical gain at a certain (threshold) current must balance the optical loss of the cavity:

$$g_{th} = \frac{1}{\Gamma}[\alpha_i + \alpha_m] = \frac{1}{\Gamma}[\alpha_i + \frac{1}{2L} ln\left(\frac{1}{R_1 R_2}\right)] \quad (2.1)$$

Where g_{th} is the threshold gain and Γ is the optical confinement factor (overlap between the active region and optical field). α_i and α_m are internal and mirror loss of the cavity, respectively. L is the cavity length, R_1 and R_2 are top and bottom DBRs reflectivities [3], [7].

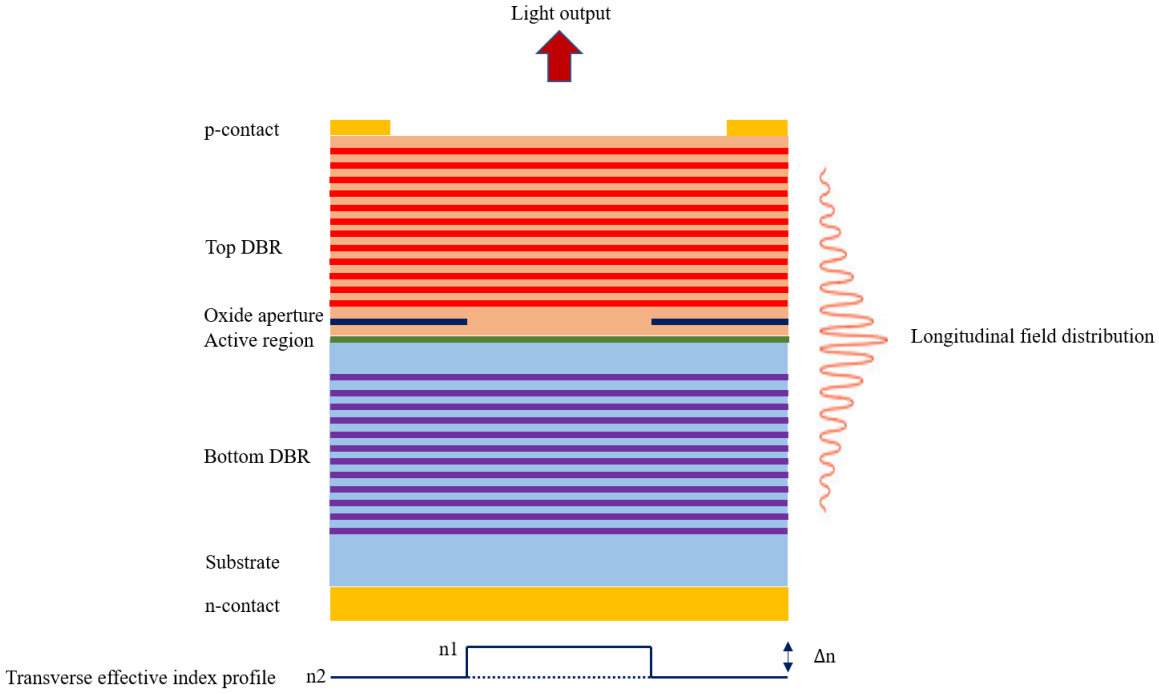

Figure 2.3: Schematic cross section of a VCSEL with transverse effective index profile.

A semiconductor laser as a p-n junction needs to be under a forward bias for optical gain and therefore stimulated emission. p-contact located on the top DBR and n-contact positioned beneath the bottom DBR provide requirements for current injection through the VCSEL. The VCSEL operates under either continuous wave (CW) or pulsed current injections. Figure 2.4 presents an example of pulse current. Duty cycle is defined as the ratio of the pulse width to the pulse period. When the VCSEL is under a

forward bias, electron and hole pairs are condensed in the active region where radiative transition and recombination take place. Increasing current injection results in more population inversion and therefore higher optical gain [3], [7]. The lasing starts at a certain current (threshold current) where the round-trip gain compensates the round-trip loss.

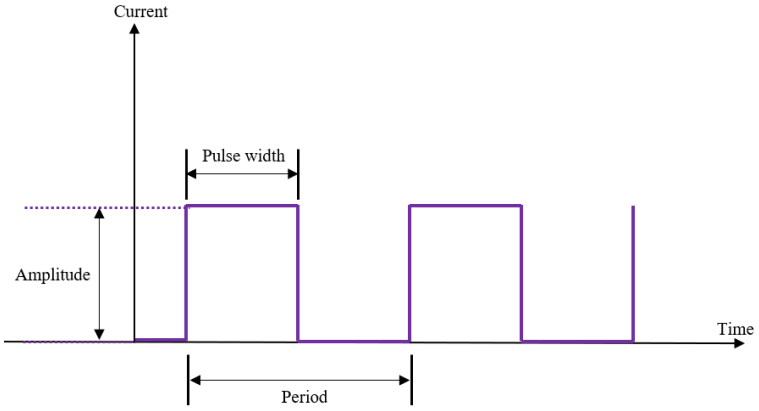

Figure 2.4: Pulsed current.

2.1.1 VCSELs: Features and applications

VCSEL is one of the most important lasers among the semiconductor lasers due to some advantages compare to other semiconductor lasers including high modulation bandwidth at low injected currents, high efficiency at low output powers, high reliability, and temperature operating range [8]. The market demand of VCSELs is dramatically increasing due to couple of reasons which are mentioned briefly in introduction part of the thesis. Main applications of VCSELs are mostly related to communication (data centers), sensing and measurements.

There are few necessities to have in VCSELs to use it in sensing or measurement applications e.g. being capable of focusing the beam on diffraction limited spot, high power for having accurate and quicker measurements, and also sometimes polarization stability under current and temperature alterations. One of the most useful applications in sensing area, can be optical navigation e.g. optical computer mouse and optical fingerprint tracking. In addition, gas sensing, atomic clocks, blood glucose monitoring, and motion sensing in mechanical setups are some examples of the sensing application [6]. However, VCSELs can be used as illumination source in LiDARs, automotive systems, imaging, and sensing the objects in 3 dimensional (3D) spaces. High power and efficient VCSELs with almost uniform far field and optimized divergent beam are essential in 3D sensing applications [2], [4], [5].

Another favourable application of 850-1060 nm VCSEL is in optical communication system, specifically short-reach distance of transmission. In moderate distance communication, single mode VCSELs emitting at 1310 nm and 1550 nm can be used to prevent fibre loss, pulse broadening and have perfect coupling to the fibre. In shorter distance communications for instance in optical networks in data centres and high-performance computers, 850 nm VCSELs are utilized as the dominant light source due to their high speed, efficiency, and low cost [6].

2.2 Optical resonant cavities

Like all lasers, resonator is a part of VCSELs in which both longitudinal and transvers modes are given rise. Every transverse mode has a specific intensity distribution and therefore specific beam properties [7]. Design of the cavity length of VCSELs are considerably different from cavities of edge emitting lasers. The VCSEL cavity length is simply on the order of the one wavelength and due to the huge spacing between longitudinal modes, there is only one longitudinal mode in a VCSEL which also shows the emission wavelength. Therefore, the VCSEL can be called single longitudinal mode laser.

Considering effective step index and the oxide aperture size of the VCSEL, the transverse modes can be defined and explained. Also, they can be calculated via Helmholtz equation with known geometry and border conditions [9]. The transverse modes in VCSELs can be introduced with LP_{mn} modes as shown in figure 2.5 which are extracted from BeamGage software. Radial and azimuthal mode index, the intensity distribution of modes, are defined by n and m. Theoretically and experimentally, the output intensity distribution will be superposition of all beams generated by modes, which is also discussed and measured in this thesis. The generation of modes has a certain order. In a VCSEL, LP_{01} is the first and fundamental mode with Gaussian distribution. An example of orders in generated modes will be discussed later in this thesis, as well.

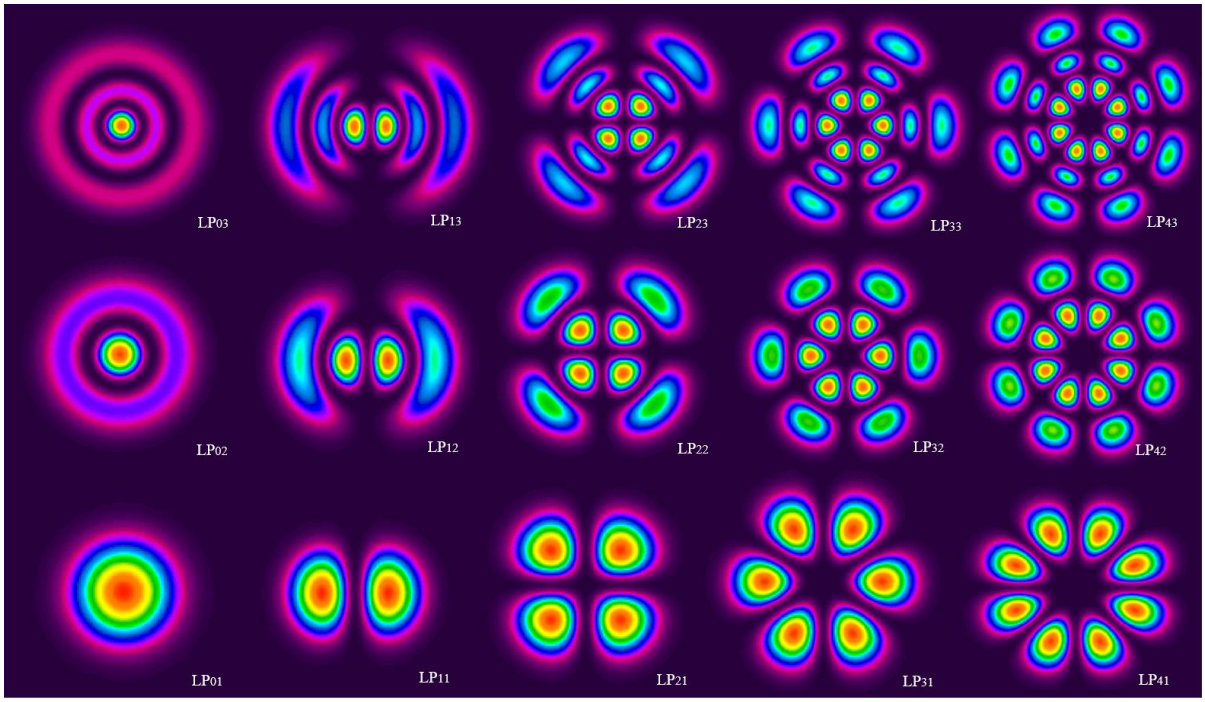

Figure 2.5: Optical intensity near-field distribution in two dimensions showing transverse modes of an optical resonant cavity which can estimated by LP modes. These optical intensity distributions are created by BeamGage Professional software.

2.3 Near-field and Far-field

Literally, near-field is referred to an approximately planar wave front of light beam where is generated and exited from a laser. Then, far-field is referred to the light after some propagation which turns its

planar form to almost curvature wave front [10]. LP_{mn} modes shown in figure 2.5 are near-field modes which are created by Beamgage Professional software. Any propagation distance from the laser e.g., a few millimeters to a few centimeters or even few meters (e.g., 1.5 m in He-Ne laser) is considered as a far-field propagation [7],[11]. In this thesis, the beam profile imaging measurements are done in 33.8 mm distance between the VCSELsurface and diffuser plate which is in far field range for the VCSEL.

2.4 Single- and multi-mode VCSELs

The easiest way to control spectral width and propagated transverse modes of the VCSEL beam is to either increase or decrease the oxide aperture size of the VCSEL. To have a single mode VCSEL, the oxide aperture size needs to be small enough ($\sim$4 μm of diameter). Therefore, only fundamental Gaussian mode can propagate out. However, there will be increasing trend in differential resistance and therefore self-heating in the single-mode VCSEL which will affect the performance specially in higher environmental temperatures [12]. On the other hand, one way to have a multi-mode VCSEL is to increase the oxide aperture size in fabrication. This leads to having higher order modes in addition to the fundamental gaussian-mode [5]. Reduced self-heating and achieving more output power are two main factors in multi-mode VCSELs that can be highly useful in some specific applications like 3D-sensing, face recognition and LiDARs. In addition, fabrication for multi-mode VCSELs is easier (than single-mode) in which there is a less sensitivity to mode-selection and optical feedback [6].

2.5 Modal properties

As it is illustrated in figure 2.3, VCSEL's main parts are top DBRs (p-type), oxide aperture, active region (QWs), and bottom DBRs (n-type). One can also see the transverse effective index profile due to higher refractive index in oxide aperture as core in comparison to other layers as claddings. This leads to creation of an optical cylindrical waveguide with oxide aperture core diameter of d_{ox} and effective index difference of Δn_{eff} to confine the beam (optical field) in transverse direction [6], [9]. With current injecting either CW or pulsed, the performance in this waveguide will be affected by the generated electron-hole pairs and VCSEL self-heating due to the VCSEL resistance. On the other hand, increasing in carriers will result in increasing the guided modes. However, refractive index is dependent on the temperature to some extend referring to thermo-optic effect, which helps confining the beam to the core. Thus, this will let higher order modes be confined in the waveguide. Moreover, there is an anti-guiding effect (plasma effect) which is due to the decreasing of refractive index with increasing the electron-hole pairs (carriers). Totally, modal properties and characterization of a VCSEL is determined by these effects in the waveguide inside the VCSEL [6].

2.6 Beam width and divergence

VCSELs are designed to have a small output aperture (oxide aperture) which diffracts the emitted beam and therefore causes higher divergence. Hence, measuring the divergence in VCSELs is very important

issue. To calculate the divergence, we need to first find the best and optimum way to calculate the beam width and diameter.

By considering the nature of Gaussian beam, it never vanishes theoretically, it is not possible to estimate the beam width or divergence by the point in which the beam intensity is zero. Therefore, there are few mathematical methods shown in figure 2.6 to calculate almost accurate divergence of the beam e.g. FWHM, $1/e^2$, D4σ [13].

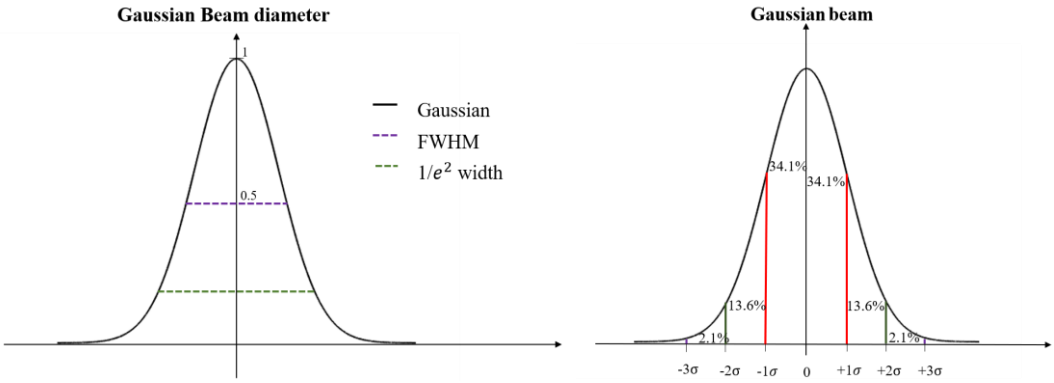

Figure 2.6: Gaussian beam distribution. FWHM and $1/e^2$ methods (left) and D4σ method (right) to calculate Gaussian beam divergence.

In $1/e^2$ method, the beam width and divergence are estimated by selecting two points where the beam intensity drops to $1/e^2$ of the peak intensity. In this method, only 86% of the whole beam intensity can be considered [13].

Full wave half maximum (FWHM) is a similar way but a little different from $1/e^2$ to calculate the beam width. In this method, the beam diameter is recognized by selecting two points from 1D or 2D beam output where the intensity reaches to half-peak value [13].

In D4σ method, the Gaussian intensity distribution is divided by 4σ (-2σ, -1σ, 0, +1σ, and +2σ), figure 2.6 (right). It has a high, satisfying, and realistic accuracy in many cases that is proved by ISO standards and able to cover about 95.4% of the light beam in the calculations [13]. Despite the high accuracy in D4σ, it is very challenging and has complicated definitions so basically researchers rarely choose it for their measurements. Luckily, there is a chance to apply this method to some measurements and imaging softwares like BeamGage that makes the beam profiling very straight forward and accurate.

After estimating the beam diameter (assume to be d(z), where z and z_0 are coordination and beam waist position, respectively), we will be able to calculate the divergence which happens to the beam while travelling through space. The spreading out of the beam like a cone that is called divergence, can be calculated mathematically by:

$$\theta = \lim_{(z-z_0)\to\infty} 2.\tan^{-1}\left(\frac{d(z)}{2(z-z_0)}\right) \tag{2.5}$$

In this equation, θ is full angle of the diverged beam.

Furthermore, there are a few methods for estimating the beam divergence experimentally e.g. focal length, far-field wide angle, and far-field two points which all are based on the beam diameter. The divergence angle in these methods are literally referred to half angle of the diverged beam cone.

2.6.1 Focal length method

In this method with a certain beam spot size (diameter) of d(z), the divergence can be calculated by:

$$\theta = \tan^{-1}(\frac{d(z)}{f}) \tag{2.6}$$

In this equation, f is the focal length of the imaging optic system that can be added manually to the BeamGage software for divergence calculations. The point is that, the calculated beam diameter which results in the divergence angle is related to the diameter of the beam in focal length of the lens not the diameter of collimated beams after the focal length. With being aware of this beam diameter, the software is able of calculating the divergence angle.

2.6.2 Far-field wide angle

This method is also for using experimentally in the software. The only factor that is needed to be known and added is the distance of the diffuser plate (connected to the imager) from VCSEL surface. In this case, the equation for calculating the divergence with known beam diameter is:

$$\theta = 2.\tan^{-1}(\frac{d(z)}{2.z_0}) \tag{2.7}$$

In this equation, z_0 is the mentioned distance. So, there is no need to relocate the camera for extra measurements and keeping stationary fixed is enough for this method of calculations.

2.6.3 Far-field two points

In this method, the estimation of the divergence is done with knowing two beam diameters in two different locations. Therefore, we need to relocate the camera or the light source to have second beam diameter as well. The parameters which are required to be implemented in the software are beam spots in two various points in addition to the distance between these points. Then, the divergence is defined with following equation:

$$\theta = 2.\tan^{-1}(\frac{d_2(z)-d_1(z)}{2.z_0}) \tag{2.8}$$

where $d_1(z)$ and $d_2(z)$ are first and second camera distances from the laser, respectively [13].

2.7 Why 940 nm VCSEL?

Black body radiation of the sun is shown in figure 2.7. By comparing the solar black body radiation outside of the atmosphere with the one inside the atmosphere (sea level), we can see that there are a few absorptions in certain frequencies. These absorptions are caused due to various substances in the atmosphere e.g. O_3, O_2, H_2O, CO_2 or etc. With looking close to around 940 nm in the spectrum, there is a considerable dip due to the absorption of the solar radiation by water droplets or humidity in the

air. This absorption provides few benefits which helps in a great performance of this VCSEL for 3D-sensing applications and more specifically for outdoor applications like LiDAR, face recognition in mobiles or other applications in cars. One of the advantages is that if we use a 940 nm VCSEL, there will be less background noise and lightening than other frequencies, since the atmosphere will filter out wavelengths ranging around 940 nm. On the other hand, a silicon-based sensor is sensitive in this frequency rather than other frequencies in the solar spectrum. In addition, silicon is also one of the cheapest sources to be used in the sensors and cameras. Finally, one essential advantage of using this frequency is that it is very safe for human and living animals [14].

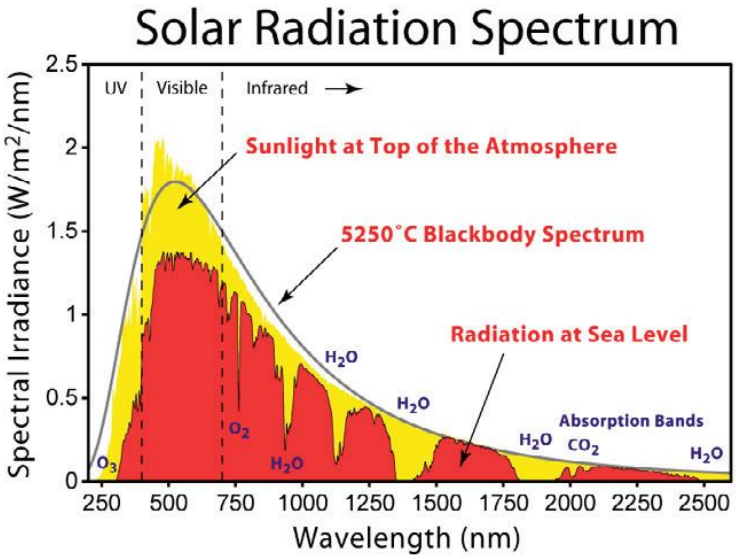

Figure 2.7: Black body radiation of the sun and solar spectrum outside the atmosphere and at the sea level [15].

3. Methods

In this thesis, modal characterization of 940 nm VCSELs under continuous wave and pulsed current operations and at different ambient temperatures are investigated. Current-power-voltage (IPV) characteristic, optical spectrum and beam profile measurement are three main sections covered experimentally in this chapter.

3.1 IPV measurement setup with integrating sphere

The theory behind this setup is measuring a VCSEL output power by a Si-based photodetector. When an emitted photon hit the detector an electron-hole pair is generated and therefore results in a current (photocurrent) in external circuit.

Figure 3.1 shows the IPV setup with an integrated sphere. VCSEL is probed with P-29-2550-1 probe which is located under entrance aperture of the integrating sphere. A large area Si photodetector is connected to the sphere from right hand side port.

Large area Si photodetectors are common and popular in IPV setups even without an integrating sphere. However, it is not a proper detector for large size light sources and array VCSELs with high divergence, since its aperture is not large enough to collect all emitted light. In comparison with large area Si based photodetectors, due to big entrance aperture of the integrating sphere it can easily collect almost all light coming from larger VCSELs or array VCSELs and divergent light sources. The integrating sphere that is used in this setup is IS6-C-UV with 4 ports and 170° acceptance angle for having uniform light diffusion. It is a spherical cavity with reflective interior and one entrance aperture with 63.5 mm diameter and three ports in which one port is connected to a detector and then to a computer to collect data. The input can be via fiber or free space.

In order to collect most of the light, we need to have minimized distance from the VCSEL located almost at the centre of the entrance aperture of the integrating sphere and considering a safe margin to not damage the probe or the VCSEL.

The measurements are done under temperatures of 25 ℃ to 85 ℃ by a temperature controller to investigate the performance of the VCSEL at different ambient temperatures.

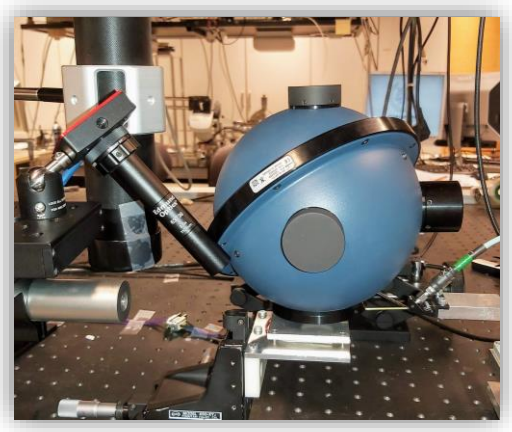

Figure 3.1: IPV setup with an integrating sphere. The Si photodetector is connected to the sphere from right hand side port.

3.2 Spectrum measurement via lens coupled setup

The setup used in this thesis to measure optical spectrum of VCSELs is shown in figure 3.2. It is formed of two lenses and an optical fiber connected to an optical spectrum analyser (OSA), figure 3.2 (left and center). The first lens collimates the VCSEL beam and the second lens focuses the beam into the fiber. The fiber is a multimode fiber (MMF) with core diameter of 50 µm and numerical aperture (NA) of 0.275. Specifications of lenses and the MMF are listed in table 3.1. The aim of the setup is coupling almost all the VCSEL beam to the MMF connected to an OSA to measure the beam spectrum, figure 3.1 (right). The VCSELs are probed with 40A-GSG-100-P probe in this setup and the VCSEL-stage is connected to a temperature controller KEITHLEY 2510.

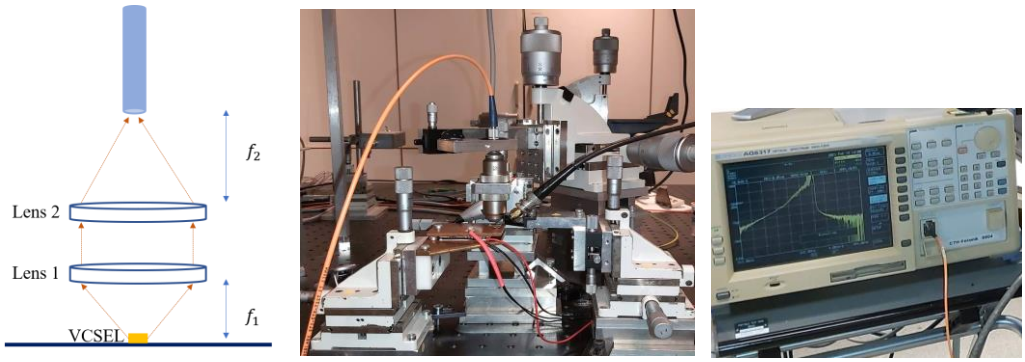

Figure 3.2: Scheme of a lens coupled setup (left), real lens coupled setup (center) and an optical spectrum analyzer (right).

Table 3.1: Characteristics of lenses and the multimode fiber used in lens coupled setup.

Component	Focal length	NA (numerical aperture)	CA (clear aperture)	M (Magnification)	Core diameter
Lens 1	8.00 mm	0.50	8.0 mm	20 X	-
Lens 2	11.00 mm	0.25	5.5 mm	16 X	-
Fiber	-	0.275	-	-	50 µm

Regarding the different current operations in this setup, the OSA will take average of the light power in the pulsed operation, since the detector in the OSA is slow. Therefore, the duty cycle of the pulse

current can be considered and apply to the averaged spectrum to calculate and plot the spectrum with real power levels. However, for further analysis, separation of modes and their relative peak to peak value in the spectrum are much more important.

One important point during the measurement of spectrum in different temperatures from 25 ℃ to 85 ℃, is misalignment of the setup due to the expansion of metals with temperature. Therefore, at each temperature the power of the light reached to the MMF needs to be checked by a power-meter and compared with the measured IPV at the same temperature and bias current. Realignment is necessary to achieve the highest coupling efficiency.

3.3 Beam profile imaging with WB-I and CCD camera

This setup consists of a wide beam imager (WB-I) positioned above the VCSEL, camera (Spiricon SP928), electrical current source (CW or pulsed), BeamGage professional software, a VCSEL, a VCSEL holder, suitable probe and temperature controller, figure 3.3. The WB-I is a long black tube with a diffuser plate at the near end and an optical imaging setup positioned the far end to the VCSEL. The WB-I is vertically positioned over the VCSEL and connected to a camera. The VCSEL beam is diffused uniformly be the diffuser plate and the optical imaging setup together with the camera capture the diffused beam profile. The camera and WB-I are vertically located of zero degrees of axis from the VCSEL beam. The VCSELs are chosen in three different oxide aperture sizes of 7.5 μm, 14.9 μm and 20.0 μm. However, the usual and best size is 7-8 μm of oxide aperture which is normally used in arrays in the industries.

The VCSEL is probed with P-29-2550-1 probe placed on a xyz-translation stage to be able to move it with micrometer precision. This probe is connected to a DC current source (KEITHLY 2400) or a pulsed current source (ILX light wave LDP-3811) through a coaxial cable. The VCSEL-stage (holder), is made of copper and connected to a temperature controller (ILX light wave 5525B) which can control temperature from -99 ℃ to 199 ℃.

The aim is to capture the VCSEL beam profile in far-field (which was explained in theory section). Therefore, the distance of 33.8 millimeter is applied between the diffuser plate and the VCSEL on the holder. The superposition of created modes at each certain current and temperature is shown in BeamGage software. The divergence is also calculated in BeamGage software and proved with two-point calculation method. The D4σ proved by ISO standards is set in the software to have highest accuracy of divergence. To eliminate background noises including the spontaneous emission and ambient noise, the setup is calibrated by using the BeamGage software.

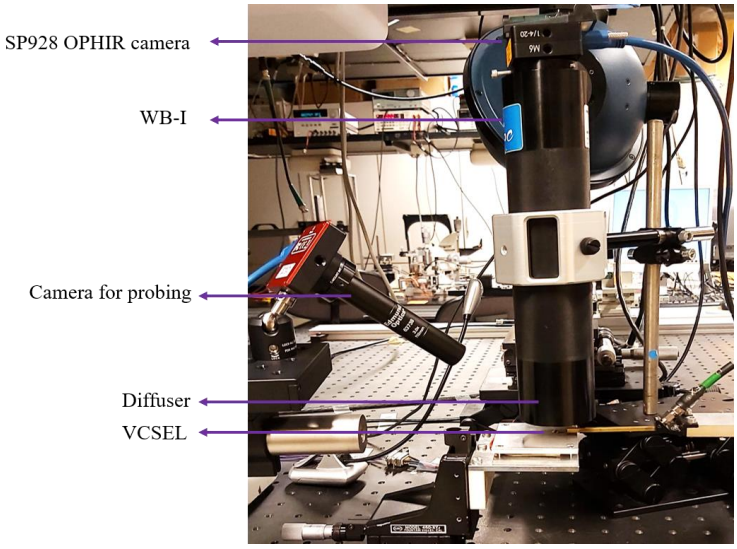

Figure 3.3: Beam profile imaging setup.

4. Results

In this chapter, the IPV, optical spectrum and beam profile characteristics of 940 nm VCSELs with different oxide aperture sizes under two current operations, CW and pulse, are discussed. Since the applications of these VCSELs are mostly outdoor and may face different ambient temperatures and conditions, so variation of temperature in each measurement and characterization is considered. The IPV is measured using the integrating sphere setup, optical spectrum by the lens coupled setup and OSA and finally, beam profile is captured by the WB-I and camera.

4.1 Characterization of VCSELs with CW current operation

The current-power (IP) performance of a 940 nm VCSEL with 7.5 µm oxide aperture is shown in figure 4.1.1. This measurement is done with integrating sphere setup and under CW current operation at different ambient temperatures from room temperature (25 °C) to 85 °C. The effect of increasing temperature is obvious in the VCSEL performance. Peak power decreases with increasing the ambient temperature. While, the threshold current (the current where gain and loss of the cavity are equal) increases with rising the temperature which is not good from power consumption perspective. Peak power and threshold current values at different temperatures are listed in table 4.1.

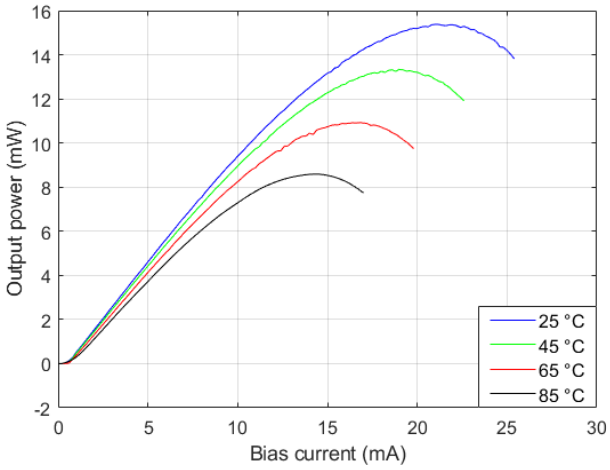

Figure 4.1.1: IP of a 7.5 µm VCSEL with CW current operation at different temperatures.

Table 4.1: Threshold current and peak power of a 940 nm VCSEL with 7.5 µm oxide aperture and CW current operation at different temperatures.

Temperature	**25 °C**	**45 °C**	**65 °C**	**85 °C**
Threshold current (mA)	0.522	0.546	0.625	0.757
Peak power (mW)	15.4	13.3	10.9	8.6

Afterwards, optical spectrum of the VCSEL is measured by the lens coupled setup and the OSA. The spectrum of the VCSEL with 7.5 µm oxide aperture at just above threshold current at 1 mA and different temperatures are illustrated in figure 4.1.2. Usually, VCSELs with oxide aperture larger than 4 µm are multi-mode, as it is the case in this VCSEL as well. The fundamental mode is generated earlier than the

other modes and has the highest power at this current level (1 mA) in comparison with other mode at all four temperatures. However, the performance of the VCSEL is getting weaker (less power) with increasing the temperature and therefore peak value of the modes decrease and the modes shift to longer wavelengths (red-shift). The reason of shifting spectrum to longer wavelengths is that cavity expands optically (Refractive index depends on the temperature) and becomes longer with increasing the temperature. Therefore, the resonance wavelength of the cavity becomes longer.

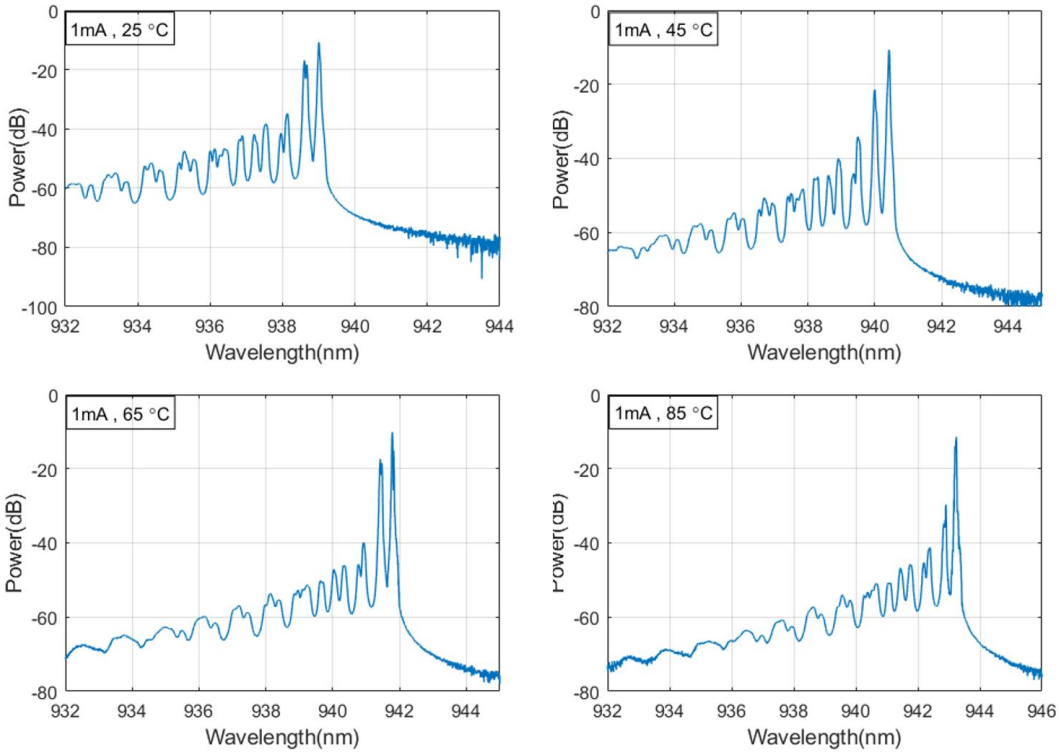

Figure 4.1.2: Optical spectrum of a 7.5 µm VCSEL at 1 mA CW operation and at different temperatures.

One reasonable operation current is somewhere in the middle between the threshold and roll-over currents (where the maximum power happens). Therefore, performance of this VCSEL at 12 mA CW operation is also measured and shown in figure 4.1.3. This range of current operation is needed to have more created higher order modes with high enough power, however it results in self-heating. Likewise, there is a clear wavelength shift to longer wavelength at higher ambient temperatures.

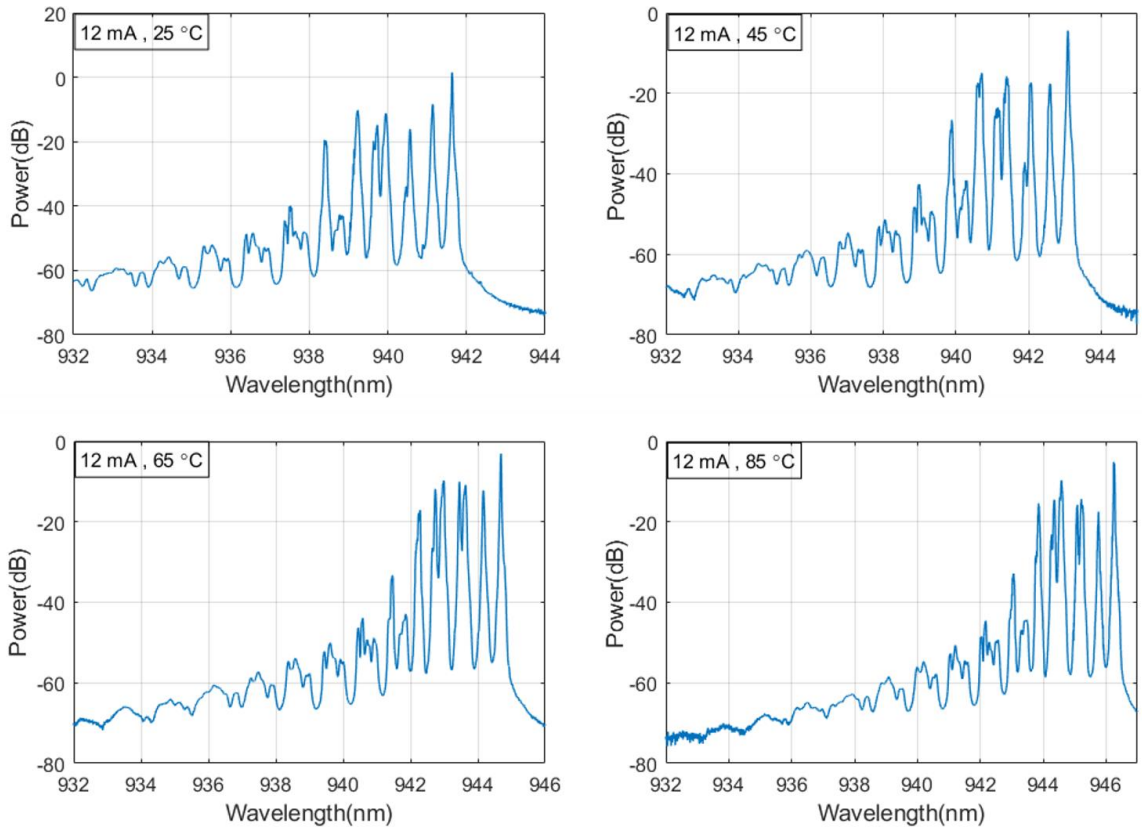

Figure 4.1.3: Optical spectrum of 7.5 µm VCSEL at 12 mA CW operation and at different temperatures.

IP of two larger VCSELs with 14.9 µm and 20 µm oxide aperture diameters are also characterized and shown in figure 4.1.4. Both VCSELs have higher power than 7.5 µm VCSEL due to the larger oxide aperture and therefore a larger gain medium.

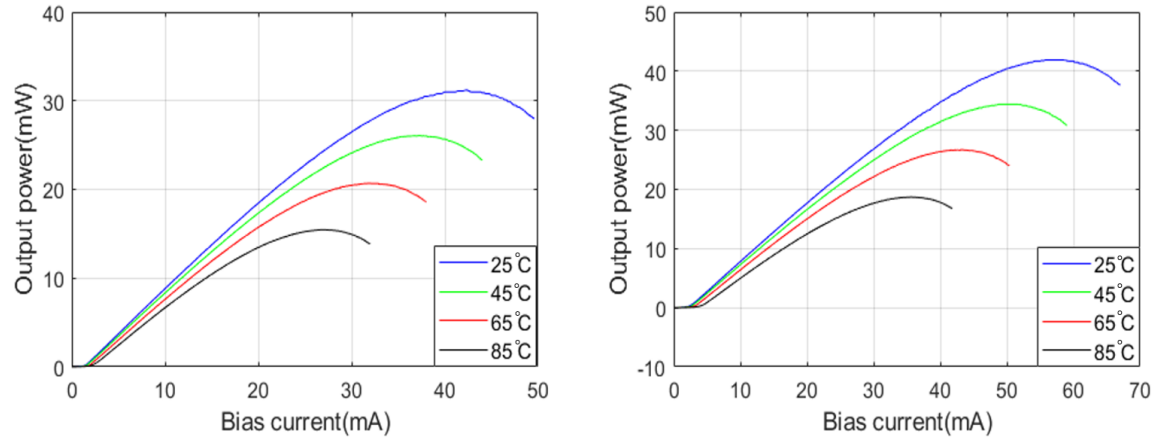

Figure 4.1.4: IP characteristics of 14.9 µm (left) and 20 µm (right) oxide aperture VCSELs with CW operation and at four different temperatures.

The spectrum for 14.9 µm and 20 mm VCSELs show much more modes than 7.5 mm VCSEL. Like the 7.5 µm VCSEL, all modes red-shift by increasing the temperature, figures 4.1.5 and 4.1.6. Tracking the wavelength of the fundamental mode of the 14.9 µm VCSEL, shows a red-shift from 940.7 nm at 25 ℃ to 945.3 nm at 85 ℃.

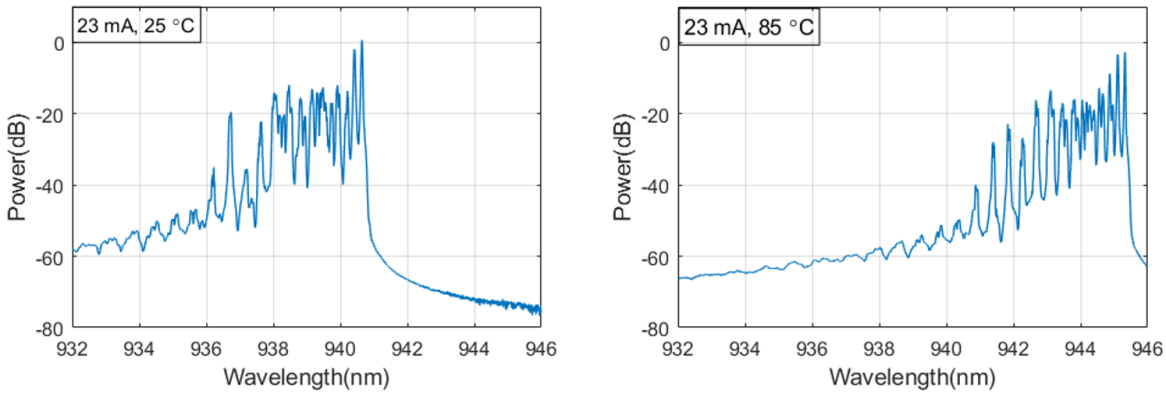

Figure 4.1.5: Optical spectrum of 14.9 µm VCSEL at 23 mA CW operation at two different temperatures of 25 °C (left) and 85 °C (right).

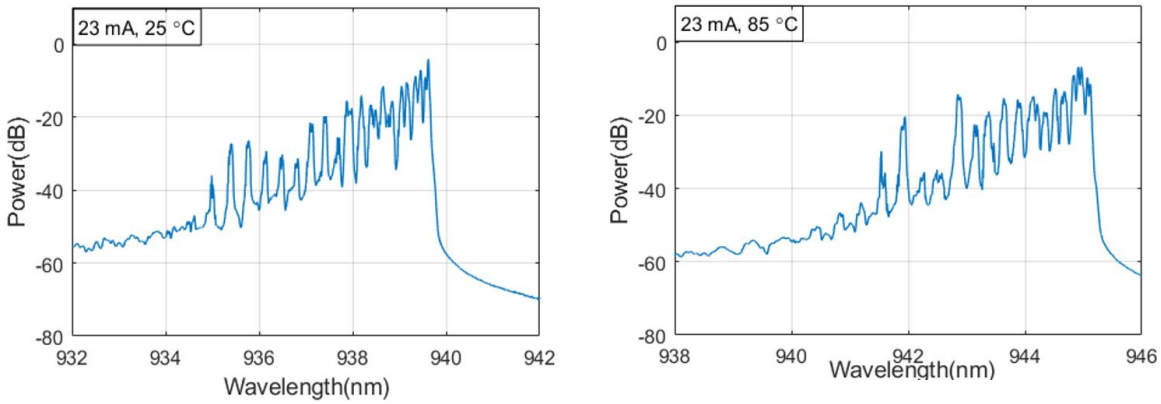

Figure 4.1.6: Optical spectrum of 20 µm VCSEL at 23 mA CW operation at two different temperatures of 25 °C (left) and 85 °C (right).

Differential resistance is another important parameter of VCSELs and is defined as $\frac{\Delta V}{\Delta I}$. This factor is calculated for each VCSEL with 7.5, 14.9 and 20 µm oxide apertures by extracting current and voltage from IPV measurements, figure 4.1.7. As it is shown, the resistance of the smallest VCSEL is higher than other VCSELs. In a very simple way, the resistance is defined as R= $\rho \frac{l}{A}$, where R and ρ are resistance and resistivity of the VCSEL, respectively. L is the height (or length) of the VCSEL and $A=\pi.r^2$ is the area of the oxide aperture with radius r. In addition to this simple explanation, current funneling due to a small oxide aperture is the main reason of the VCSEL resistance. The resistance of VCSELs increases with temperatures, figure 4.1.7.

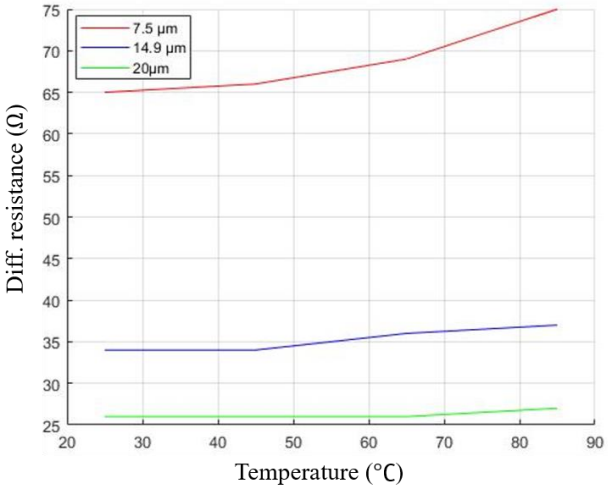

Figure 4.1.7: Differential resistance of three VCSELs with different oxide apertures vs. temperature.

For the VCSEL with oxide aperture of 7.5, 14.9 and 20 µm, the wavelength shift of the fundamental mode as a function of temperature at different CW currents, 12, 20 and 33 mA, respectively, is shown in figure 4.1.8. All VCSELs show a linear increase in wavelength with rate ~0.075 nm/°C.

Variation of the fundamental mode wavelength as a function of dissipated power in each VCSEL at two different ambient temperatures (25 °C and 85 °C) are plotted in figures 4.1.9-4.1.11. Dissipated power is the amount of the power which is lost as mainly heat inside the VCSEL. It can be calculated by subtraction of the electrical input power (I.V) and the optical output power (measured by integrating sphere setup), equals to RI^2 and results in VCSEL self-heating. Where, R is the VCSEL resistance and I is the bias current. Figures 4.1.9-4.1.11 prove that the wavelength of the fundamental mode shifts linearly with dissipated power.

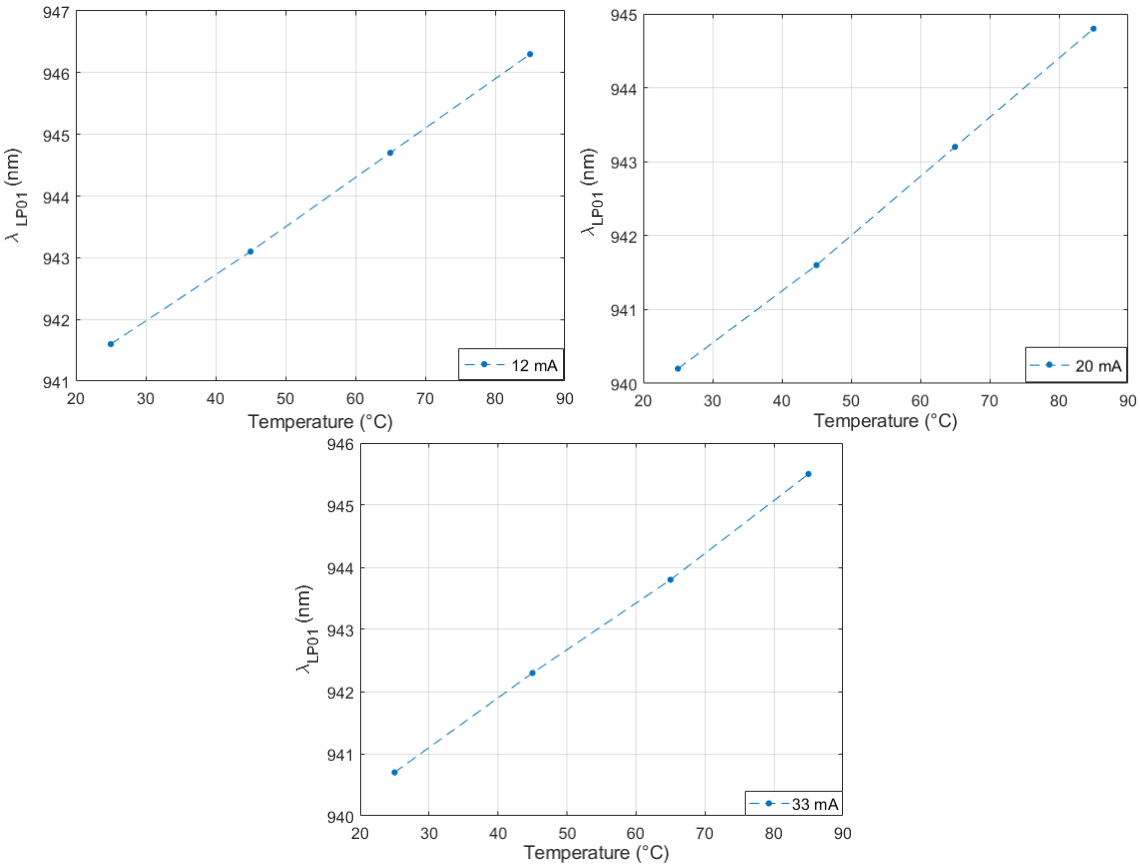

Figure 4.1.8: Wavelength shift of the fundamental mode as a function of temperature for 7.5 µm VCSEL at 12 mA CW current (top left), 14.9 µm VCSEL at 20 mA CW current (top right) and 20 µm VCSEL at 33 mA CW current (bottom).

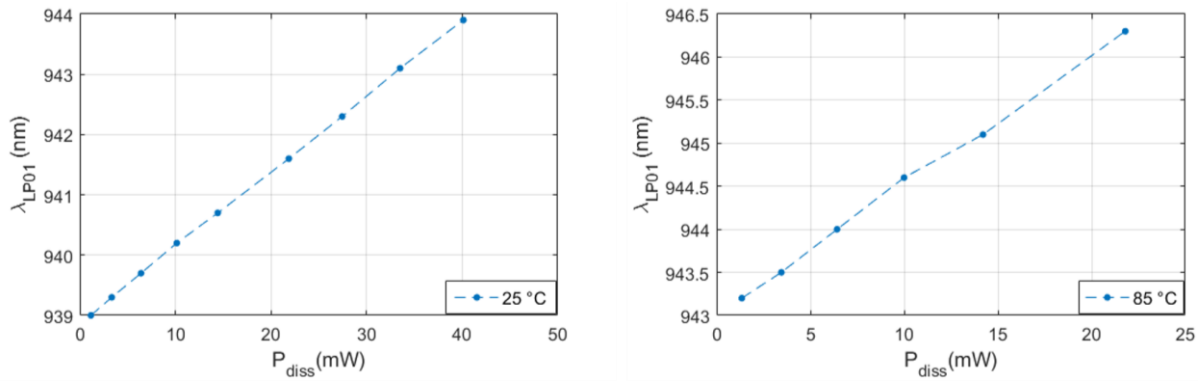

Figure 4.1.9: Fundamental mode wavelength shift vs. dissipated power for 7.5 µm VCSEL at two different temperatures 25 $°C$ (left) and 85 $°C$ (right).

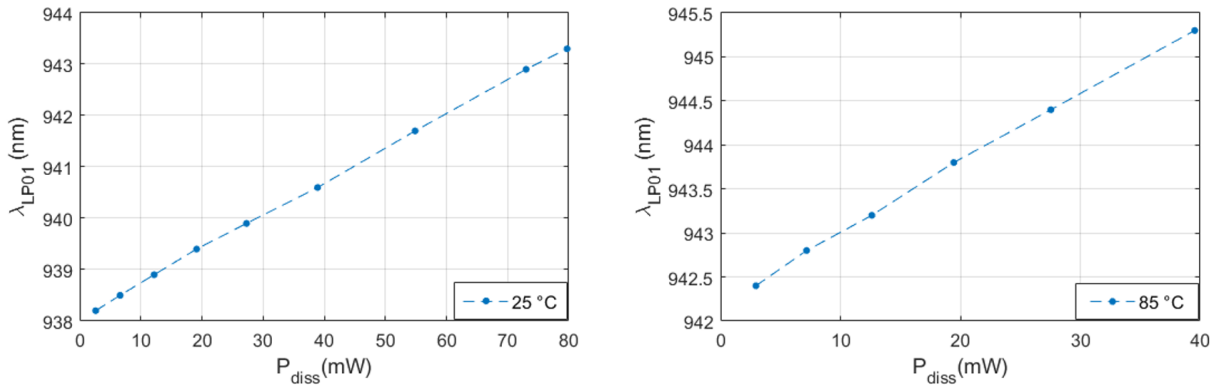

Figure 4.1.10: Fundamental mode wavelength shift vs. dissipated power for 14.9 µm VCSEL at two different temperatures 25 °C (left) and 85 °C (right).

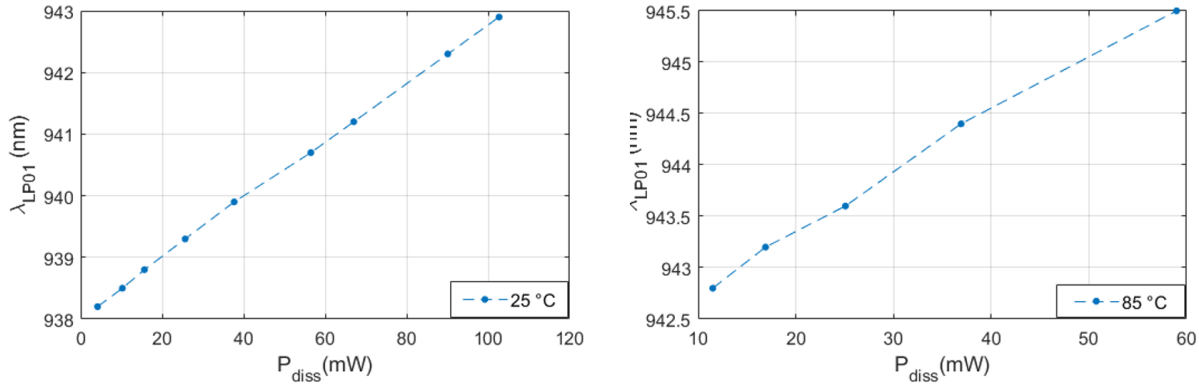

Figure 4.1.11: Fundamental mode wavelength shift vs. dissipated power for 20 µm VCSEL at two different temperatures 25 °C (left) and 85 °C (right).

Table 4.2 summarizes wavelength shift of the fundamental mode as a function of temperature and dissipated power for all three VCSELs.

Table 4.2: wavelength shift of the fundamental mode as a function of temperature and dissipated power for all VCSELs.

VCSEL size (µm)	$\Delta\lambda/\Delta P_{diss}$ $(nm/mW)(25\ °C)$	$\Delta\lambda/\Delta P_{diss}$ $(nm/mW)(85\ °C)$	$\Delta\lambda/\Delta T$ $(nm/°C)$
7.5	0.116	0.1496	0.075
14.9	0.0691	0.0741	0.070
20	0.043	0.0561	0.080

In VCSELs, thermal impedance is defined as the amount of changes in temperature by changing the dissipated power. Equation 4.1 shows how we can define the thermal impedance.

$$Thermal\ impedance = R_{th} = \frac{\Delta T}{\Delta P_{diss}} = \frac{\Delta\lambda/\Delta P_{diss}}{\Delta\lambda/\Delta T} \quad (4.1)$$

To estimate thermal impedance of a VCSEL, we need to use data from variation of wavelength (fundamental mode is selected in this thesis) vs. dissipated power and vs. ambient temperature. From figures 4.1.9 to 4.1.11 we can calculate $\Delta\lambda/\Delta P_{diss}$ ratio for VCSELs with oxide aperture of 7.5 µm, 14.9 µm and 20 µm, respectively. Ratio of $\Delta\lambda/\Delta T$ also can be obtained from figure 4.1.8. The calculated

thermal impedances for different VCSELs at two different temperatures are listed in table 4.3. The table states that larger VCSEL has smaller thermal resistance and also it increases by the temperature.

Table 4.3: Thermal impedances of the VCSELs ($\Delta T/\Delta P\_diss(°C/mW)$) at two different temperatures.

VCSEL size (µm)	**25 °C**	**85 °C**
7.5	1.546	1.9946
14.9	0.9871	1.059
20	0.5375	0.70125

Another interesting point is the wavelength shift as a function of the bias current. By increasing the bias current, wavelength of the fundamental mode become longer. For the 7.5 µm VCSEL and at 25 ℃, wavelength of the fundamental mode is 939 nm at 1 mA and shift to 944 nm at 18 mA. Figure 4.1.12 shows the wavelength shift of the fundamental mode as a function of bias current at 25 ℃ for three different VCSEL sizes. The reason of parabolic shape in these three figures is shifting of the wavelength to longer wavelengths with increased temperature caused due to dissipated power. On the other hand, dissipated power is equal to RI^2 which proves that wavelength increases parabolically with current.

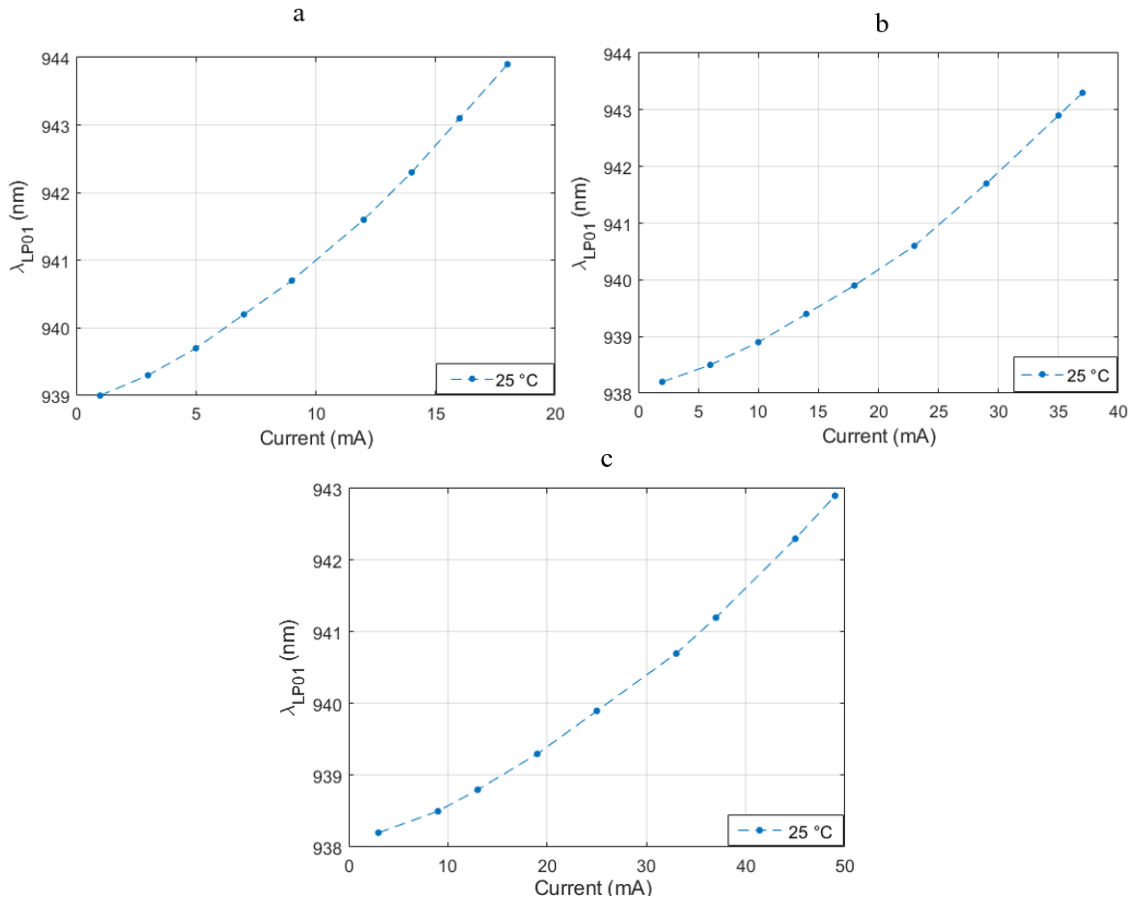

Figure 4.1.12: Fundamental mode wavelength as a function of CW current at 25 °C for (a) 7.5 µm VCSEL, (b) 14.9 µm VCSEL and (c) 20 µm VCSEL.

To be able to track the relation of optical output power to electrical input power in our selected VCSELs, we need to calculate the power efficiency of VCSELs. The power efficiency of VCSEL with different oxide aperture are calculated and plotted at four different temperatures based on the measurements and

input parameters, figure 4.1.13. This illustrates the rising of power efficiency up to a certain point at each temperature then it decreases with different slopes in each temperature (higher temperatures drop faster). The maximum power efficiency stands for a specific current point for running the VCSEL in the most efficient way. From figure 4.1.13 it is deduced that a VCSEL has a quite efficient performance for currents from just above the threshold to the half roll-over. At higher temperatures, VCSEL has lower output power and therefore lower efficiency. The power efficiency is obviously higher in smallest VCSEL (0.44 at 25 ℃) in comparison with other two large VCSELs and the reason is that referring to equation 4.2 the ration of output power to input electrical power is higher.

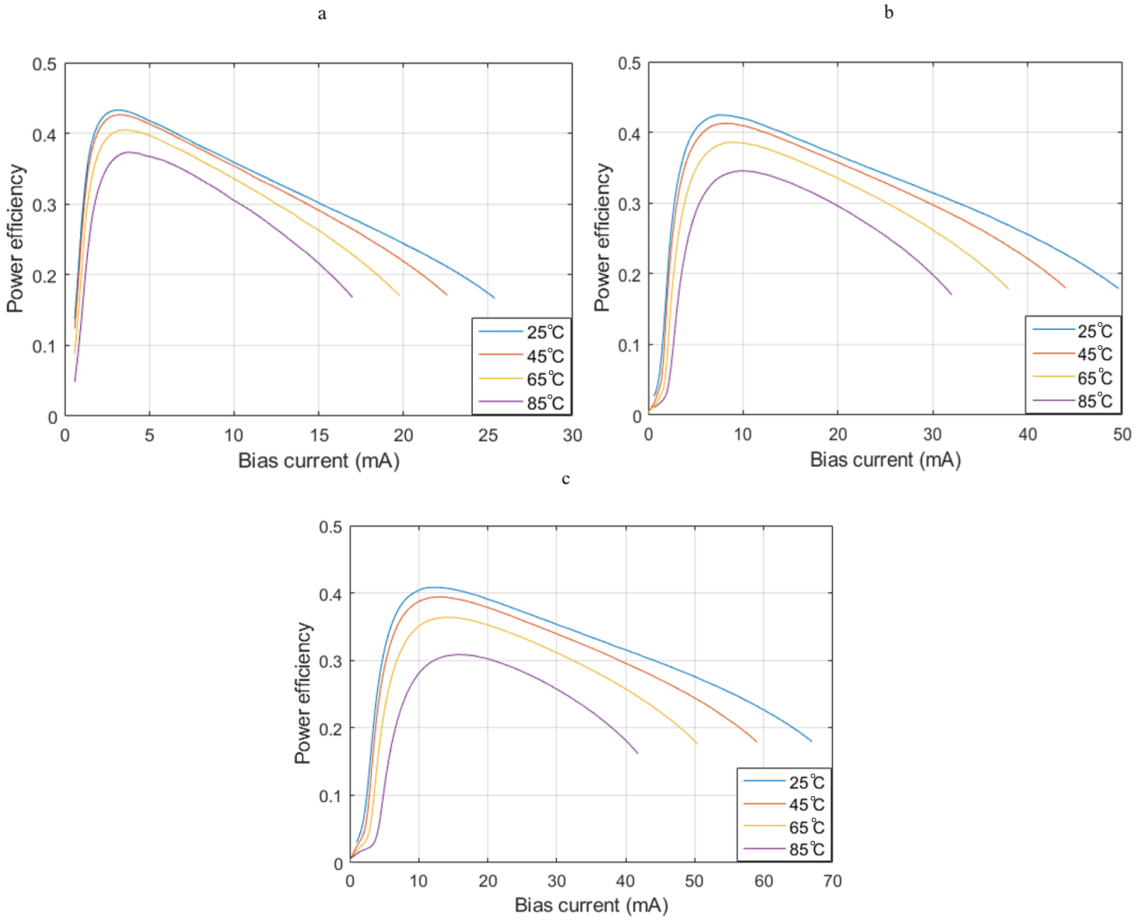

Figure 4.1.13: Power efficiency vs. bias current at different ambient temperatures for (a) 7.5 μm VCSEL, (b) 14.9 μm VCSEL and (c) 20 μm VCSEL.

$$\eta_p = \frac{P_{out,opt}}{P_{in,elec}} = \frac{P_{out,opt}}{V.I} \tag{4.2}$$

Where, η_p is the power efficiency and $P_{out,opt}$ and $P_{in,elec}$ are optical output and electrical input powers, respectively. I is the bias current and V is the voltage of the VCSEL at each specific current.

4.2 Characterization of VCSELs with pulsed current operation

As it was mentioned in previous sections, the other current source is pulsed source. Pulse width, duty cycle and its amplitude (value of bias current) are three variables in this measurement. Another external variable is the ambient temperature provided by temperature controller connected to the VCSEL-stage varying from 25 °C to 85 °C. However, we can only investigate one variable at the same time. So, in one occasion, different pulse widths (PW) at a constant temperature (25 °C) and another occasion a constant pulse width at different temperature. Figure 4.2.1 shows the performance of a VCSEL with 7.5 µm oxide aperture at 25 °C and a fixed duty cycle of 1% with different pulse widths. The maximum output power with pulsed current operation is for pulse width of 0.1 µs which is about 4.5 times more than operating with CW current at the same ambient temperature. This means that operating the same VCSEL with pulsed current lets the VCSEL feel less self-heating which avoids reducing the output power. On the other hand, smaller pulse width is preferred to avoid the self-heating effect inside the VCSEL and let VCSEL to be cool down between two short pulses.

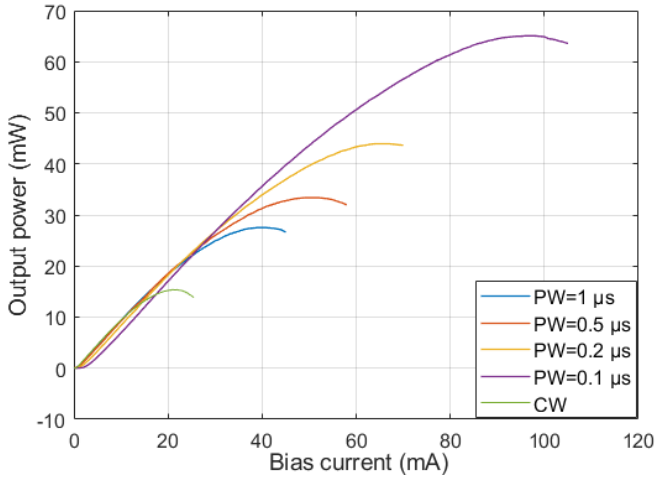

Figure 4.2.1: IP of 7.5 µm VCSEL in different pulsed widths of pulsed current operation at DC=1% and T= 25 °C.

The second measurement with pulsed source is to consider constant pulse width = 0.1 µs and DC= 1% with varying ambient temperature at 25 °C, 45 °C, 65 °C and 85 °C. In figure 4.2.2 you can see the result of IP measurement for this explained condition. Even though the pulse operation helps a lot with self-heating issue, the effect of heating can be again seen in figure 4.2.2 at 85 °C in which the output power is almost 20 mW lower in roll-over than in 25 °C. The output power in 85 °C in worst case with pulsed current is around 46 mW, while it is only 8.6 mW in the CW current.

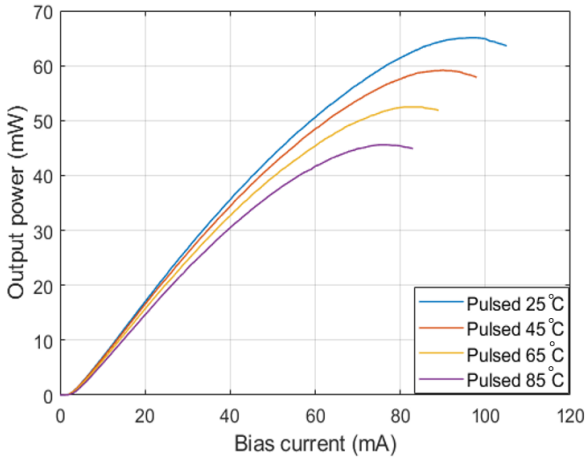

Figure 4.2.2: IP of 7.5 µm VCSEL in 0.1 µs pulse width and DC=1% of pulse current operation at different temperatures.

Considering some larger oxide aperture VCSELs with 14.9 µm and 20 µm, the difference of operation in continuous wave current source and pulse current source is shown in figure 4.2.3. As it was previously mentioned and discussed about larger aperture sizes of VCSELs, they can have higher output power compared to smaller one. With 0.1 µs of pulse width, duty cycle of 3 % and varying temperature, the measured output power with integrating sphere setup shows us a dramatically different output power for pulsed and CW operation.

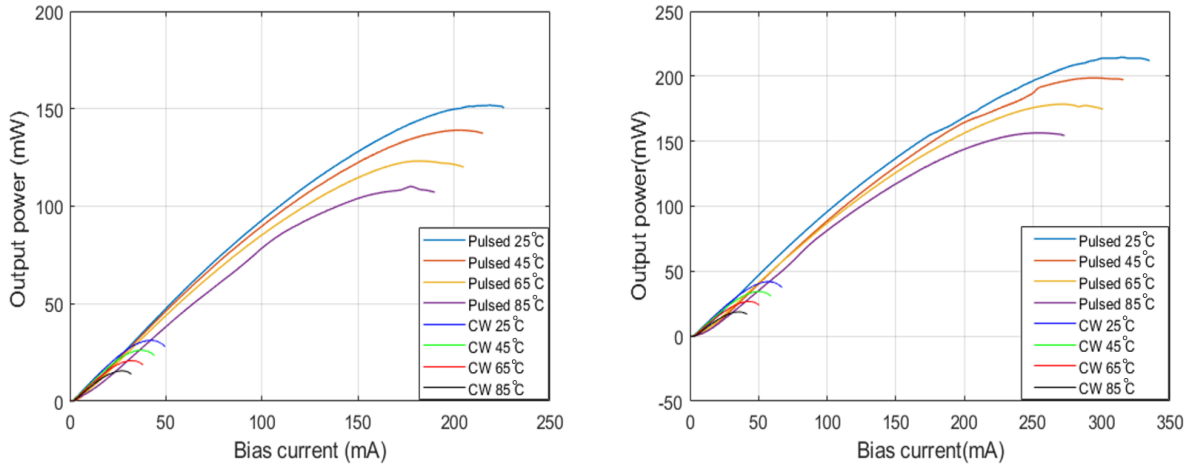

Figure 4.2.3: IP of 14.9 µm (left) and 20 µm (right) oxide aperture VCSELs with pulsed operation with PW=0.1µs and DC=3% compared to CW operation.

Considering different pulse widths, as it was explained previously in this chapter, figure 4.2.4 shows us the spectrums of 7.5 µm oxide aperture VCSEL operating at 2 mA pulsed current source with DC = 1% and at 25 °C. Despite having higher output power within shorter PW (0.1 µs), the spectrum measurement with lens coupled setup at PW = 0.1 µs shows less generated modes with lower peak power. This means in longer pulses, the VCSEL has enough time to run longer and create more modes.

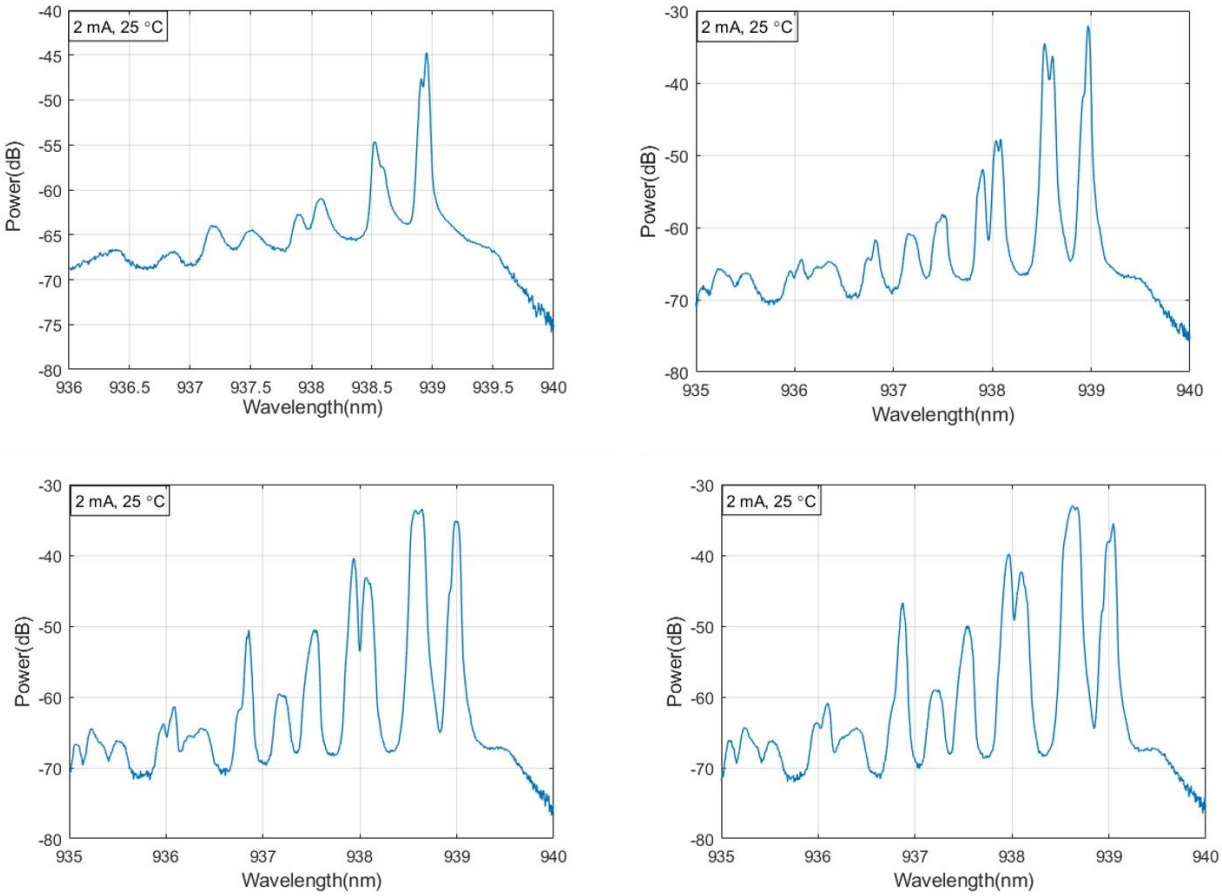

Figure 4.2.4: Spectrum of 7.5 µm oxide aperture VCSEL operating at 2 mA pulsed current, 1% of DC and different pulsed widths, 0.1 µs (top left), 0.2 µs (top right), 0.5 µs (bottom left), 1 µs (bottom right).

By considering constant PW= 0.1 µs and DC= 1%, the spectrum measurements were done at different temperatures and at 12 mA pulsed current operation, see figure 4.2.5. Decreasing power level, lower number of generated modes, and wavelengths shifting to longer wavelengths are some significant effects of increasing temperature from 25 °C to 85 °C in this measurement. However, mode spacing of fundamental mode and 2nd order mode is one important point which is almost fixed ~0.4 nm at all temperatures and both pulsed and continuous wave current operations, see figures 4.2.5 and 4.1.3. In these two figures, VCSEL is run at 12 mA in 4 various temperatures with pulsed and CW sources, respectively.

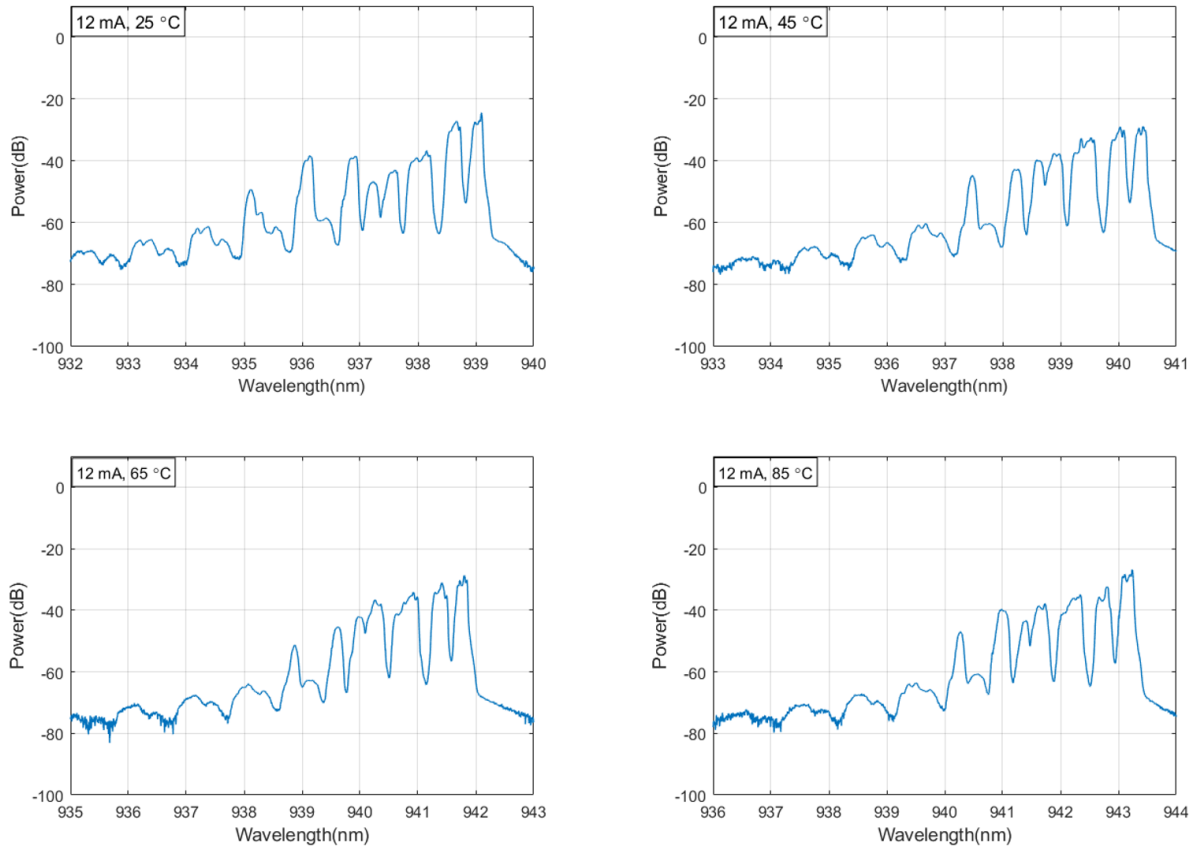

Figure 4.2.5: Spectrum of 7.5 µm oxide aperture VCSEL operating at 12 mA pulsed operation with 0.1 µs pulse width and 1% of DC at four different temperatures.

4.3 Beam profiles

The last part of measurements is related to beam intensity profile imaging which is done with a wide beam imager as explained in previous chapter. Figure 4.3.1 shows measured beam intensity profiles of 7.5 µm oxide aperture VCSEL at both CW (upper row) and pulsed current operation with PW = 0.1 µs and DC= 3% (lower row) and at different temperatures. These profiles illustrate the superposition of generated modes and indicates beam intensity with referring to color bar attached to each measurement in which red color shows us the highest intensity and dark purple shows lowest intensity. One critical point during the measurements to be considered, was that we needed to be careful about saturation which is usually monitored in BeamGage professional software in white color inside the taken image. Another point is that the calibration is equally done for these eight beam profiles in figure 4.3.1 which helps us to compare them easily. The calibration before measurements is required to do, since we need to first filter out the background noise and have a same intensity level in all measurements for one VCSEL. With comparing spectrum measurements of this VCSEL shown in figures 4.2.5 and 4.1.3 we can see the superposition of generated modes in figure 4.3.1. The divergence is calculated by both software and manual calculations which is applied on profile images (dashed lines) starting from 5 ° of half divergence angle. The divergence of the beam increases in lower ambient temperature which means the divergence in CW operation at 25 °C is more than at 85 ° C. The reason is that the output power is

more in lower temperatures so we will have more modes and more power levels to reach the camera. Distance of 33.8 millimeter is applied between the VCSEL surface and the diffuser plate.

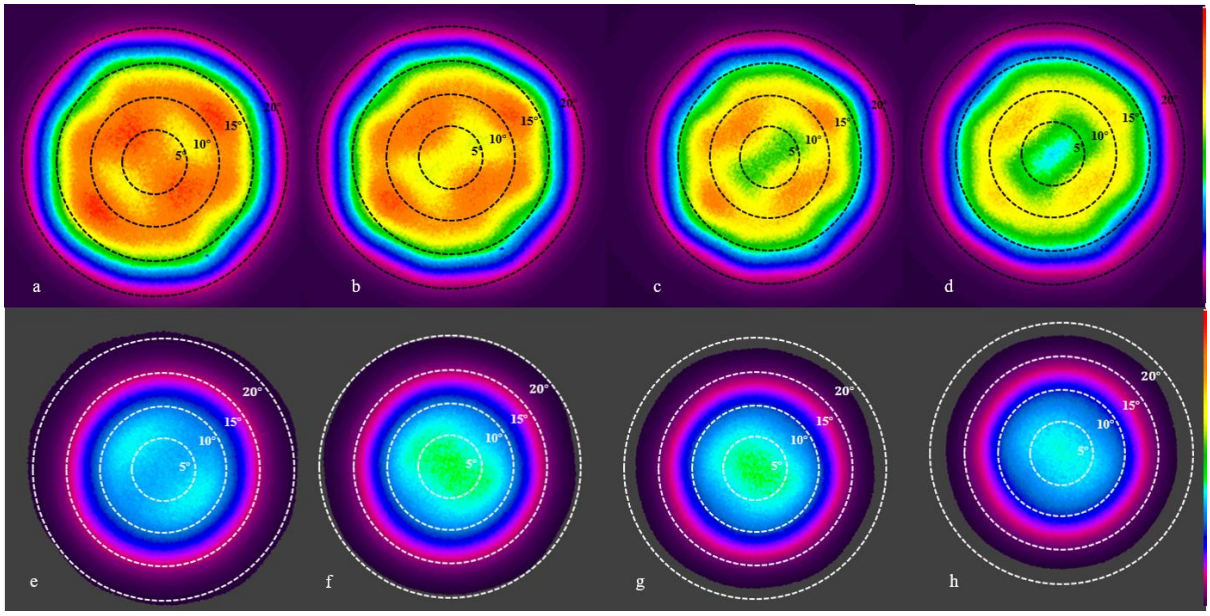

Figure 4.3.1: Beam intensity profiles of the 7.5 µm VCSEL (upper row) operating at 12 mA CW and at (a) 25 °C, (b) 45 °C, (c) 65 °C and (d) 85 °C. (lower row) Operating at 12 mA pulsed operation with DC 3 % and pulse width of 0.1 µs at (a) 25 °C, (b) 45 °C, (c) 65 °C and (d) 85 °C. The color bar is not equal for two operations since an attenuator, ND1, (10% transmission and 90% absorption) is used in CW case. Dashed lines show azimuthal coordination.

One point about using CW current source in this measurement is that due to higher output power we must use attenuators before the camera to reduce receiving power. Otherwise, the camera will be saturated. While, in pulsed current operation, the camera (which is slow) take an average of the power and therefore there is no need for an attenuator. Table 3.1 lists optical attenuators used to capture the intensity profile of different VCSELs in CW current operation. Here, ND1 means it transmits only 10% of the incoming light and ND2 means it transmits 1% of the incoming light.

Table 3.1: Utilized optical attenuators to measure the beam profiles of the different VCSELs in CW operation.

VCSEL size (µm)	ND1 (10% transmission)	ND2 (1% transmission)
7.5 µm	✓	-
14.9 µm	-	✓
20 µm	-	✓

Figure 4.3.2 illustrates beam profile of a VCSEL with 14.9 µm oxide aperture diameter running at 23 mA in two- and three-dimensional formats. The interesting point is lower power at 85 °C, which is well shown in 3D format. The profile in 85 °C is tilted to have a better view of the influence of temperature on performance of the VCSEL. However, having larger oxide aperture size have also playing a deteriorating effect on performance of the VCSEL. For instance, in a VCSEL with a large oxide aperture, 20 µm here, it is difficult for current to reach the center part of the oxide aperture. Therefore,

there will be donut-shape beam, like figure 4.3.3, where there is not enough power intensity in the center. However, this is not an issue in smaller VCSELs.

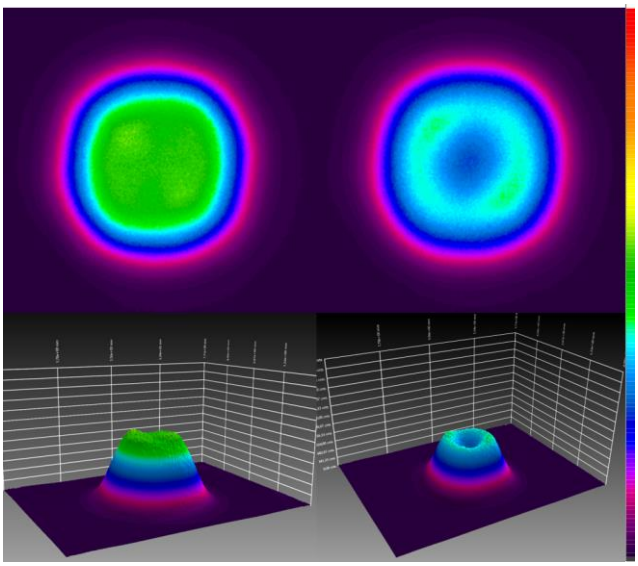

Figure 4.3.2: 2D (top row) and 3D (bottom row) beam intensity profiles of a 14.9 µm oxide aperture VCSEL running at 23 mA CW current operation at 25 °C (left column) and 85 °C (right column).

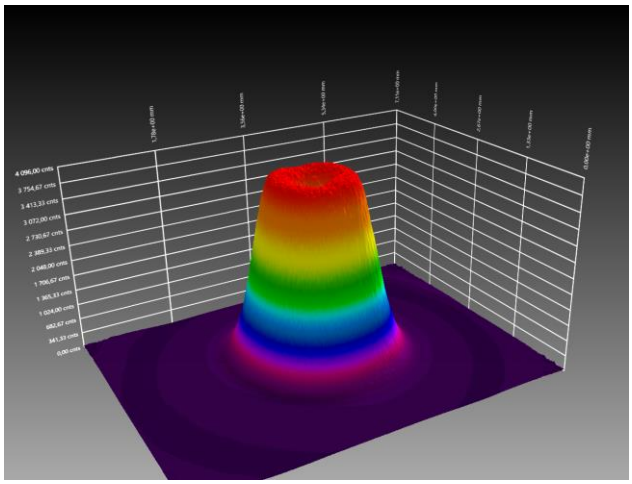

Figure 4.3.3: 3D beam profile of a VCSEL with 20 µm oxide aperture running at 23 mA CW current operation and 25 °C.

5. Conclusion

In this thesis modal characterization of 940 nm VCSELs with the purpose of use in 3D sensing applications have been investigated. IPV performance, optical spectrum, and beam intensity profile of VCSELs with different oxide aperture diameters, 7.5 µm, 14.9 µm, and 20 µm at different temperatures have been measured and studied. All the measurements are done under CW and pulsed current operations.

Measurements show that a VCSEL with larger aperture has a higher output power, while it has a lower power efficiency. For a specific size of a VCSEL, increasing the ambient temperature results in a higher threshold current, lower slope efficiency and therefore lower output power.

Furthermore, for a specific VCSEL at a specific ambient temperature, increasing the bias current leads to more self-heating of the VCSEL due to the VCSEL resistance and therefore sooner roll-over current. In general, any increase in temperature, ambient temperature, or self-heating, degrades a VCSEL performance.

To avoid self-heating and for 3D-sensing and LiDAR applications, pulsed current operation is studied. In this case, the VCSEL has enough time to be cool down between each two successive pulses and avoids self-heating. It has been shown that pulses with a fixed duty cycle and smaller pulse width result in a higher output power. Moreover, VCSELs at a same pulse width and duty cycle at different temperatures were studied. Here, higher ambient temperature decreases the output power. However, in pulse current operation the output power is much higher than the CW operation.

Optical spectrum investigation done by couple lensed setup together with wide-beam-imager setup, revealed that at a specific current, larger VCSELs support more modes. In a specific VCSELs, higher current results in more modes at the output. Increasing the ambient temperature decreases the number of modes and also makes the output beam less divergent. In the pulse operation, either higher duty cycle or higher pulse width result in more modes.

Another outcome of the thesis is to choose an appropriate size (oxide aperture) of singlet or array VCSELs that are being used for 3D-sensing application. For a singlet, a VCSEL with 7-8 µm oxide aperture diameter is suggested. Since, this size of a VCSEL has higher efficiency than larger devices. Very large devices, e.g., 20 µm should be avoided due to inefficient pumping of the fundamental mode. Although small VCSELs are efficient, they have less output power. Therefore, array of small VCSELs can provided power needed for long distance LiDAR applications.

For future, array VCSELs including small VCSELs (7-8 µm) can be characterized and studied for this aim. In addition, beam profile in far-field can also be simulated for different VCSELs at different currents, temperatures, and different pulse operations and be compared with the experimental study.

6. Bibliography

[1]: Jahed, Mehdi, Johan S. Gustavsson, and Anders Larsson. "Precise setting of micro-cavity resonance wavelength by dry etching." Journal of Vacuum Science & Technology B, Nanotechnology and Microelectronics: Materials, Processing, Measurement, and Phenomena 37.3 (2019): 031217.
[2]: Seurin, Jean-Francois, et al. "High-efficiency VCSEL arrays for illumination and sensing in consumer applications." Vertical-Cavity Surface-Emitting Lasers XX. Vol. 9766. International Society for Optics and Photonics, 2016.
[3]: Haglund Erik, 2015, 'VCSELs for high-speed, long-reach and wavelength-multiplexed optical interconnects', PhD thesis, Chalmers University of Technology, Gothenburg.
[4]: Moench, Holger, et al. "VCSEL-based sensors for distance and velocity." Vertical-Cavity Surface-Emitting Lasers XX. Vol. 9766. International Society for Optics and Photonics, 2016.
[5]: Okur, Serdal, et al. "High-power VCSEL arrays with customized beam divergence for 3D-sensing applications." Vertical-Cavity Surface-Emitting Lasers XXIII. Vol. 10938. International Society for Optics and Photonics, 2019.
[6]: Larsson, Anders. "Advances in VCSELs for communication and sensing." IEEE Journal of selected topics in quantum electronics 17.6 (2011): 1552-1567.
[7]: Persson Anton, 2018, 'Beam characterization of VCSELs', Master thesis, Chalmers University of Technology, Gothenburg.
[8]: Hashemi Seyed Ehsan, 2012, 'Relative intensity noise (RIN) in high-speed VCSELs for short reach communication', Master thesis, Chalmers University of Technology, Gothenburg.
[9]: Larsson Anders, 2010, 'Semiconductor optoelectronics', Department of Microtechnology and Nanoscience, Chalmers University of Technology.
[10]: Coldren, Larry A., Scott W. Corzine, and Milan L. Mashanovitch. Diode lasers and photonic integrated circuits. Vol. 218. John Wiley & Sons, 2012.
[11]: [Online]. Available:
https://www.photonics.com/Articles/Beam_Diagnostics_Meeting_the_Need_for_High/a25162
[12]: Haglund, Erik, et al. "Reducing the spectral width of high-speed oxide confined VCSELs using an integrated mode filter." Vertical-Cavity Surface-Emitting Lasers XVI. Vol. 8276. International Society for Optics and Photonics, 2012.
[13]: [Online]. Available: https://www.ophiropt.com/blog/laser-measurement/calculate-laser-beam-size.
[14]: Dummer, M., et al. "The role of VCSELs in 3D sensing and LiDAR." Optical Interconnects XXI. Vol. 11692. International Society for Optics and Photonics, 2021.
[15]: Wu, H. W., et al. "Design and fabrication of an albedo insensitive analog sun sensor." Procedia Engineering 25 (2011): 527-530.

7. List of VCSELs

VCSEL	Oxide aperture diameter [µm]	Singlet	Array
6B9 0940-8: R3C1	7.5	yes	-
6B9 0940-8: R7C16	14.9	yes	-
6B9 0940-8: R8C16	20	yes	-

DEPARTMENT OF Microtechnology and Nanoscience
CHALMERS UNIVERSITY OF TECHNOLOGY
Göteborg, Sweden 2021
www.chalmers.se